Investigations of Anharmonic Low-Frequency Oscillations in Heme Proteins[†]

Florin Rosca, Anand T. N. Kumar, Dan Ionascu, Xiong Ye, Andrey A. Demidov, Theodore Sjodin, David Wharton, Douglas Barrick,[‡] Stephen G. Sligar,[§] Takashi Yonetani,[∥] and Paul M. Champion*

Physics Department and Center for Interdisciplinary Research on Complex Systems, Northeastern University, Boston, Massachusetts 02115

The technique of femtosecond coherence spectroscopy is applied to a variety of photostable and photochemically active heme protein samples. With the exception of cobalt-substituted myoglobin, strong oscillations are detected near 40 cm^{-1} in all of the samples studied. Additional modes near 80, 120, and 160 cm^{-1} are observed in the photochemically active samples. The amplitude and phase behavior of the low-frequency modes are studied by tuning the pump/probe carrier wavelength across the Soret absorption spectrum. A simple harmonic model is not able to account for the observed relative intensities of these modes or the carrier wavelength dependence of their frequency and phase. As a result, we develop an anharmonic model where the oscillatory signal is damped as the result of heterogeneity in the potential surface. The underlying source of the heterogeneity in the anharmonic potential surface is found to be correlated with the inhomogeneous broadening of the Soret band. The presence of the higher harmonics in the photochemically active samples demonstrates that the anharmonic mode is strongly coupled to the ligand photodissociation reaction (i.e., upon photolysis it is displaced far from equilibrium). Moreover, the observation of the ∼40 cm^{-1} oscillations in all of the iron-based heme protein samples, including porphine and protoporphyrin IX model compounds, suggests that this mode is associated with nuclear motion of the core of the porphyrin macrocycle. Since normal mode calculations and prior kinetic models predict the frequency of the heme "doming mode" to be near 50 cm^{-1}, we suggest that the reaction coupled oscillations at ∼40 and ∼80 cm^{-1} are a direct reflection of anharmonic heme doming dynamics. Evidence for coupling between the heme doming dynamics and the Fe−His stretching mode is also presented.

I. Introduction

Femtosecond coherence spectroscopy (FCS) is a pump/probe technique that utilizes the spectral bandwidth associated with ultrafast laser pulses to prepare and monitor coherent states in resonant and nonresonant samples.[1−12] This technique allows the real-time observation of ultrafast processes, so that the initial phases of the detected vibrational oscillations can be measured and compared. Following the pump pulse excitation, two types of processes can occur that we refer to as "field driven" and "reaction driven". In the first case, the pump pulse excites the Raman active modes of the sample without affecting its structure. In the "reaction driven" case, the photoexcited state rapidly decays, via nonradiative channels, into a coherent "product state". In both cases, the delayed probe pulse monitors the pump-induced transient absorption changes in the sample.

In this work, we focus on the detection and characterization of time-resolved low-frequency vibrational modes in heme proteins. The heme proteins form a large class of biomolecules, which are involved in a variety of important biochemical reactions such as diatomic ligand storage and transport, enzyme catalysis, and electron transfer. The heme group (active site) is a planar chromophore containing iron, which is bound to the "proximal" histidine (His) in Mb and to a cysteine (Cys) in cytochrome P450. The iron atom, at the center of the heme group, can reversibly bind diatomic molecules such as NO, CO, and O_2, which can in turn be photolyzed by a femtosecond laser pump pulse. The relaxation dynamics of the nonequilibrium structure generated by the ligand photodissociation reaction has been extensively studied over a wide range of time scales using a variety of techniques.[13−24] Here, we use FCS to study heme proteins such as myoglobin (in native, cobalt substituted, and mutant forms), hemoglobin, cytochrome P450$_{CAM}$, cytochrome c, and an iron protoporphyrin IX (FePPIX) model compound.

Ligand photolysis excites low-frequency heme/protein oscillations that arise from the forces associated with electronic rearrangements in the iron d-orbitals that take place when the iron atom undergoes a spin transition upon ligand dissociation.[6,12] These low-frequency modes are also potentially connected to energy transport and signal transduction between the active site and the protein backbone and can thus affect the physiological functionality of the protein. One particular vibrational degree of freedom that we have suggested[25−27] is highly relevant to the ligand binding and dissociation reaction is heme "doming", which corresponds to heme motion that changes the local equilibrium position of the iron atom. The iron atom changes from an in-plane position, when the diatomic ligand is bound, to an out-of-plane (∼0.4 Å) position in the

Low-Frequency Oscillations in Heme Proteins

J. Phys. Chem. A, Vol. 106, No. 14, 2002 **3541**

unligated state,[28] which is distributed and dependent on the surrounding protein conformation.[25−27] Normal mode calculations[29−31] and analysis of the nonexponential ligand rebinding[23] in Mb predict[25−27] that heme doming oscillations in the unligated state mode should be near 50 cm^{-1}.

In this work, we present data displaying a strong vibrational mode near 40 cm^{-1}, denoted as ν_{40}, which is found in all of the iron-containing heme systems studied. Its frequency spans a 37−50 cm^{-1} range, depending on the specific heme protein sample. An analysis of the structural differences between the samples displaying the ν_{40} oscillations leads us to associate the nuclear motion of this mode with the heme macrocycle. All of the photoreactive samples display at least one additional sample-dependent vibrational mode near 80 cm^{-1}, which we denote as ν_{80}. The observation of ν_{40} in deoxy Mb and ν_{40} and ν_{80} MbNO was reported earlier[6,32] using both detuned and open band detection. Here, we study the amplitude and phase behavior of ν_{40} and ν_{80} in MbNO by tuning the pump/probe carrier wavelength across the Soret absorption band. A heterogeneous anharmonic potential model is used to simulate the oscillatory signals that give rise to ν_{40} and ν_{80} (and sometimes higher harmonics) in the power spectra of the photolyzed samples. These signals are assigned to motions associated with anharmonic heme doming dynamics.

II. Materials and Methods

We use a self-mode-locked Ti:sapphire laser (Coherent, Inc.) to generate the laser pulses used in this work. The laser generates femtosecond pulses (45−100 fs) with a 76 MHz repetition rate and carrier wavelengths between 700 and 960 nm. A 0.2 mm BBO crystal is used to double the IR light in order to obtain pump/probe pulses resonant with the Soret absorption band of the heme proteins under study (400−450 nm). We use anaerobic spinning cells (rotating at ∼1000 and ∼3500 rpm) to refresh the sample in the illuminated volume. The average power of blue light at the sample is 30 mW, which corresponds to about 0.4 nJ/pulse pair. Since a pump/probe pulse pair affects less than 1% of the sample, the possibility of buildup of the unligated species in the NO bound samples (for which the ∼100 ps geminate recombination has 96−100% amplitude) is eliminated.

The pump/probe setup has been described in detail elsewhere.[32,33] To both pump and probe the studied samples, we tune the laser carrier frequency into resonance with the strong Soret absorption band in the 400−450 nm region. This allows us to selectively probe the dynamics of the active site (heme) and its interaction with the protein. For all experiments presented in this paper, we use the open band detection scheme in which the full spectrum of the probe beam is detected by a photodiode. This detection scheme facilitates accurate phase measurements for the oscillatory signal because the autocorrelation measurement that defines the pump/probe zero time delay also uses the open band detection.

Horse heart myoglobin, horse heart cytochrome *c*, and microperoxidase (MP-8) were purchased from Sigma Chemical. Bovine hemin (FePPIX model compound) was purchased from Aldrich Chemical Co., Inc., and octaethylporphyrin (OEP) was purchased from Porphyrin Products. The hemoglobin sample was provided Prof. J. M. Manning (Northeastern University, Biology Department). The P450 sample,[34] the H93G Mb sample[35,36] (proximal histidine replaced by glycine), the cobalt-substituted Mb,[37] and porphine-substituted Mb[38] were all prepared according to standard procedures. The samples were adjusted in concentration so that the optical density at the Soret maximum was near to 1 OD in a 0.5 mm sample cell.

The ferrous- and NO-bound samples are prepared in a glovebox to prevent unwanted contamination from molecular oxygen. The ferrous species was obtained by adding 2 μL of 1 M sodium dithionite solution (ascorbic acid for cytochrome *c*) to 90 μL of buffered sample. An additional 1 μL of 1 M NaNO$_2$ solution is added to prepare the NO adduct. An alternative way to prepare the NO adduct is through the addition of NO gas at atmospheric pressure. The latter method provides a 10−100-fold higher concentration of NO in solution than the former, which affects the NO bimolecular recombination rates. The nitric oxide ligand is used in this study because it geminately rebinds to the heme iron in 10−100 ps, allowing for a complete reset of the sample prior to the arrival of the next pump/probe pulse pair.

Potassium phosphate buffer (pH 7.8, 0.1 M) is used for all samples unless otherwise indicated. The P450$_{CAM}$ was dissolved in 0.1 M, pH 7.4, potassium phosphate buffer with the addition of 1 mM d-camphor for the preparation of camphor bound P450$_{CAM}$. The Fe protoporphyrin IX (FePPIX) solution was prepared with the addition of 2-methylimidazole (2MeIm) (which coordinates to Fe) and 1.5% cetyl trimethylammonium bromide (CTAB), to prevent sample aggregation. The octaethylporphyrin (OEP) was diluted in an aqueous sodium dodecyl sulfate (SDS) detergent micellar solution,[39] with the addition of 2 M 2-methylimidazole (which coordinates to Fe). The microperoxidase-8 (MP8) solution was prepared with the addition of 1.5% detergent (CTAB), to prevent sample aggregation. The H93G sample contains 2 M 2-methylimidazole, which complexes to the heme in place of the proximal histidine ligand.

The concentration of protein is chosen so that the sample has an absorbance of about 0.6 OD at the pump wavelength in a 0.5 mm cell. Each data set is the average of 60−120 scans of the optical delay line, generated in a 2−4 h experiment. To ensure sample integrity, the absorption spectrum of the sample is measured before and after each experiment and intermediate FCS files are routinely compared in order to gauge the sample stability during the course of the experiment.

Typical measured signals for resonant samples consist of damped oscillations superimposed on a monotonically decaying background. The coherence coupling signal that dominates the signal around the zero time delay is truncated before data analysis. To generate the power spectrum associated with the time-resolved oscillatory signal, we use a linear predictive singular value decomposition (LPSVD) algorithm[40] that simultaneously fits both the oscillations and the monotonic decay. This algorithm extracts the oscillatory parameters such as frequency, phase, amplitude, and damping factors, as well as the exponential parameters of the (zero frequency) monotonic background. An alternative method of analysis involves preliminary fitting of the monotonic background using the maximum entropy method (MEM), which uses a distribution of exponential decay rate constants.[41] The residual oscillatory signal is subsequently fit using LPSVD or a Fourier transform algorithm. The fits are considered stable when both techniques generate the same power spectrum for the oscillatory signals.

III. Experimental Results

To facilitate the interpretation of the experimental results, we briefly describe the active site (heme) structure and its links to the surrounding protein. The heme (iron protoporphyrin IX) is the active site of Mb and contains a porphyrin macrocycle with substituent groups bound to it (see Figure 1). The porphyrin macrocycle is a ringed structure containing 20 carbon atoms bound to an inner ring of four nitrogens. Off the outer macro-
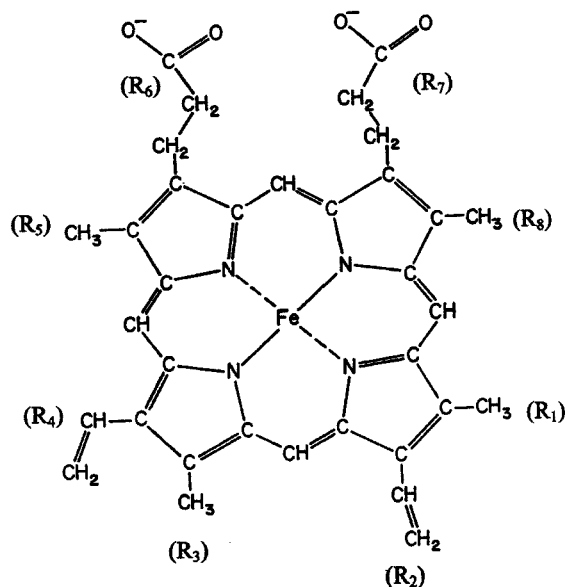
Figure 1. Structure of iron protoporphyrin IX (FePPIX). FePPIX is an asymmetric porphyrin with two vinyl groups bound at R_2 and R_4, and two propionic acid groups at R_6 and R_7.

cycle, there are eight sites where substituent groups can be bound (R_1-R_8). Iron protoporphyrin IX (FePPIX) is an asymmetric porphyrin with two vinyl groups bound at R_2 and R_4 and two propionic acid groups at R_6 and R_7. Horse heart myoglobin, hemoglobin, and cytochrome P450$_{CAM}$ all contain an FePPIX active site, which is covalently bound to the protein solely by an iron-histidine (or iron-cysteine for P450$_{CAM}$) coordination. H93G myoglobin is a myoglobin mutant for which the axial heme ligand (histidine 93) is replaced by a glycine, such that the heme−protein covalent bond is broken. In porphine Mb, the protoporphyrin IX is replaced by a porphine macrocycle with no substituent groups.[38] In horse heart cytochrome *c*, the FePPIX structure is perturbed by the thioether bridges that bind to the heme (at R_2 and R_4) from two cysteine side chains (Cys14 and Cys17). The iron atom is also coordinated to a histidine (His 18) and methionine (Met 80). Octapeptide (microperoxidase-8) is produced from the digestion of horse heart cytochrome *c* to a peptide chain of residues 14−21. The five-coordinate heme is still bound to the peptide by two thio-ether bridges but only histidine 18 coordinates to the iron atom.

A. Photostable Samples. Using the spectral bandwidth associated with the 50−100 fs pulses, we can excite and monitor vibrational modes below 400 cm^{-1}. Since we try to enhance the low-frequency part of the vibrational spectrum, we typically use the longest pulses (80−100 fs) (corresponding to the narrowest bandwidth) generated by the laser. The open band detection, in contrast to the highly detuned detection used in earlier studies,[6] also enhances the low-frequency modes.[32,42] When using photostable samples (such as deoxy Mb), the coherent oscillations are primarily induced by the forces developed during the pump pulse, which are associated with the differences between the ground and resonant excited electronic state potential energy surfaces. However, pump-induced electronic internal conversion (nonradiative population decay) processes cannot be completely ruled out as a potential source of impulsive forces that drive low-frequency modes. Since for heme proteins the resonant $\pi-\pi^*$ Soret excited state is very short-lived and the population decay takes place within 10−100 fs,[43−47] we assign the long-lived ($\sim$1−2 ps) oscillatory signals to the ground electronic state. This assignment is verified
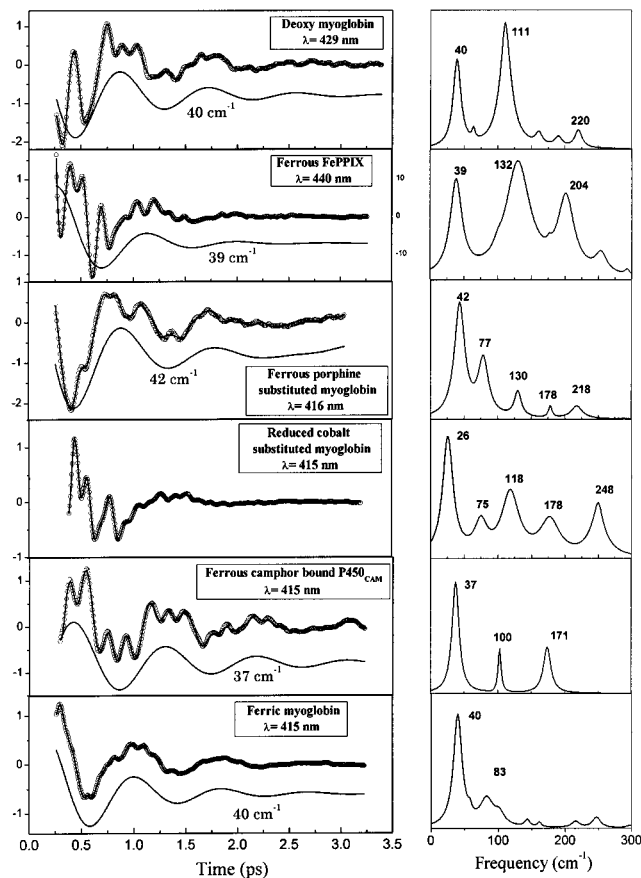

Figure 2. Sequence of experiments using the open band detection scheme on six different heme proteins. The left panels present the oscillatory part of the generated signal, and the right panels show the corresponding power spectra. The 37−40 cm^{-1} oscillation used in the fit is shown displaced from the data as a solid line. The sample and the pump/probe carrier wavelength are given in the right upper corner of the left panels.

by white light continuum measurements of the transient absorption spectrum in the Soret region.[48]

The presence of a $\sim$40 cm^{-1} mode can be clearly seen in the oscillatory signal of deoxy Mb and in the LPSVD generated power spectrum presented in the first panel of Figure 2. To characterize the heme/protein dynamics associated with this mode, we have performed experiments on a variety of other heme protein samples. Data generated in some of the other photostable samples are also displayed in Figure 2. The (statistically averaged) results obtained on all samples studied can be found in Table 1. The observation of a mode at 39 cm^{-1} in ferrous FePPIX + 2MeIm (second panel of Figure 2), which contains no surrounding protein, suggests that ν_{40} involves heme-specific motions. The faster decay (i.e., damping) of the 39 cm^{-1} mode in FePPIX compared to the 40 cm^{-1} mode of deoxy Mb also suggests that a higher degree of heme structural inhomogeneity or pure dephasing is present in the absence of protein material (see following discussion).

The presence of a 42 cm^{-1} oscillation in porphine substituted Mb (third panel of Figure 2) suggests that the source of the ν_{40} oscillation is associated with the core of the porphyrin macrocycle and does not depend strongly on the peripheral substituents. Another possible source of ν_{40}, the torsional motion of the histidine 93, appears inconsistent with the presence of modes at 43 and 39 cm^{-1} in deoxy H93G Mb and FePPIX (see Table 1). A 2-methylimidazole coordinates to the iron atom in both cases, but its torsional motion is expected to be significantly

Low-Frequency Oscillations in Heme Proteins

J. Phys. Chem. A, Vol. 106, No. 14, 2002 **3543**

TABLE 1: Summary of ν_{40} and ν_{80} in Various Heme Systems[a]

samples	ν_{40} (cm^{-1})	γ_{40}^{-1} (ps)	ν_{80} (cm^{-1})	γ_{80}^{-1} (ps)
myoglobin				
met Mb	41	0.67	82 (w)	0.4
deoxy Mb	41	0.73		
MbNO	41	0.57	81 (s)	0.49
deoxy Mb in D$_2$O	41	0.7		
MbNO in D$_2$O	41	0.54	81 (s)	0.45
deoxy Mb in 75% glycerol	41	0.71		
MbNO in 75% glycerol	41	0.65	81 (s)	0.43
deoxy H93G Mb	43	0.7		
H93G MbNO	43	0.8	87 (s)	0.33
reduced cobalt Mb			76	0.47
ferrous porphine Mb	42	0.45	76 (w)	0.56
hemoglobin				
deoxy Hb	46	0.86		
HbNO	46	0.55	91 (s)	0.35
model compounds				
ferrous FePPIX + 2MeIm	39	0.5		
ferric FePPIX + 2MeIm	37	0.5		
CO bound FePPIX + 2MeIm	44	0.53	91 (m)	0.2
ferrous OEP + 2MeIm	46	0.6		
cytochromes				
ferrous cytochrome c	44	0.53	89 (m)	0.5
ferric cytochrome c	46	0.6	95 (m)	0.46
ferrous octapeptide	50	0.6		
ferric camphor bound P450$_{CAM}$	40	0.84		
ferrous camphor bound P450$_{CAM}$	37	0.92		

[a] The estimated uncertainty for the frequencies are ± 2 cm^{-1}. The associated lifetime uncertainty is about 25%. The met Mb, deoxy Mb, and MbNO samples were run extensively, such that the results displayed for these samples are more accurate (± 1 cm^{-1}) due to better statistical averaging. The intensity of ν_{80} is compared with the intensity of ν_{40}, where s = strong, m = medium, and w = weak. The damping constant [γ^{-1} (ps)] is converted to the full width at half-maximum [γ_{fwhm} (cm^{-1})] using the expression: $\gamma_{fwhm} = \gamma/\pi c$.

different from that of histidine 93. The presence of a 37 cm^{-1} mode in ferrous P450$_{CAM}$ (fifth panel of Figure 2), in which the histidine ligand is replaced by a cysteine, definitely rules out histidine torsional motion as the source of ν_{40}.

The only sample in which ν_{40} is not obviously present (the closest detected modes are at 26 and 75 cm^{-1}) is the cobalt substituted Mb (fourth panel of Figure 2) in which the ferrous iron atom (d^6) is replaced by cobalt (d^7). This observation suggests that ν_{40} is somehow related to the electronic structure of the central metal. However, a comparison between the results obtained for the ferric (see the last panel of Figure 2) and ferrous states of Mb, FePPIX, cytochrome c, and cytochrome P450 shows that oxidation of the iron atom to d^5 does not significantly affect the frequency of ν_{40} (see Table 1).

Additional studies on samples of deoxy Mb and MbNO prepared in D$_2$O buffer and in 75% glycerol buffer display the same low-frequency mode structure as the samples prepared in normal aqueous buffer (see Table 1). Thus, we conclude that changes made to the hydration shell of the heme/protein do not have noticeable effects on the observed vibrational characteristics of the sample. The influence of the surrounding protein on the frequency of ν_{40} (ranging from 37 cm^{-1} in ferric FePPIX, to 50 cm^{-1} in ferrous microperoxidase) can be found in Table 1.

As mentioned earlier, the open band detection scheme facilitates accurate phase measurements for the FCS oscillatory signal. In addition, the inherent error of the zero time delay measurement has a smaller impact on the phases of the lower frequency modes compared to the higher frequency modes. On the other hand, the phases of the low-frequency modes are more
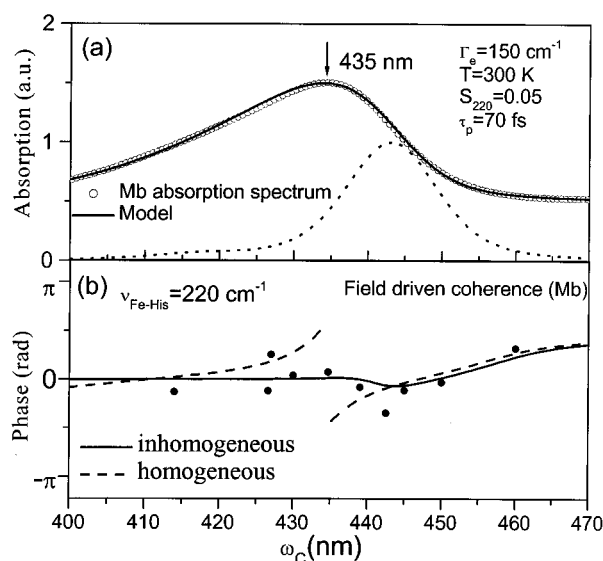

Figure 3. (a) Equilibrium absorption spectrum of deoxy Mb at $T = 300$ K (open circle) shown with the theoretical fit (solid line) based on a model for the asymmetric deoxy Mb line shape. The underlying homogeneous line shape (before the convolution with the inhomogeneous distribution) is also shown (dotted line). (b) The measured phase profile of the 220 cm^{-1} mode in deoxy Mb is presented (circles) along with two theoretical fits, based on a homogeneous (dashed line) and an inhomogeneous (solid line) model.

likely to be affected by the uncertainties associated with the smaller number of recurrences detected for low-frequency oscillations. We consider the phase measurements presented below for ν_{40} and ν_{80} to be significant within a margin of error, estimated from the phase variation ($\pm 30°$) observed for similar experimental conditions. Apart from experimental considerations that favor open band over dispersed measurements for accurate phase determination, measurements of the open band oscillatory amplitude and phase over a wide range of carrier frequencies (amplitude and phase profiles) can also help assign the origin of vibrational coherences in pump/probe spectroscopy.[49] For example, the degenerate pump/probe signal arising from a ground-state coherence has a phase profile that varies over a range of 2π as the carrier frequency is tuned across the absorption spectrum, with a sharp discontinuity between $\pm\pi/2$ at the maximum of the resonant absorption band.[49] In contrast, the excited-state phase profile, is either zero or π with a discrete phase jump at the resonant absorption band maximum.

With the above considerations in mind, we have measured the open band oscillatory amplitude and phase profiles of various modes in deoxy Mb and MbNO across the Soret absorption band. We first present, in Figure 3, the phase profile of the 220 cm^{-1} mode in deoxy Mb, over the wavelength range of 400 to 460 nm. The 220 cm^{-1} mode has been very well characterized by previous resonance Raman studies and is assigned to Fe–His stretching motion.[50] In the top panel of Figure 3, we plot the measured absorption spectrum of Mb along with a theoretical fit based on a previously proposed model for the underlying inhomogeneous distribution of electronic transition energies.[26,51] All resonance Raman active modes are included in the model, with coupling strengths determined from their absolute resonance Raman cross-sections.[52,53] The degenerate pump/probe calculations are carried out using the effective linear response approach[49] with a linearly displaced harmonic oscillator model for the vibrational modes. In Figure 3b, we plot the (open band) phase profile of the 220 cm^{-1} mode. The theoretical prediction for the phase of the 220 cm^{-1} mode in the ground state is shown for both the inhomogeneous line shape model[26,51] as well as
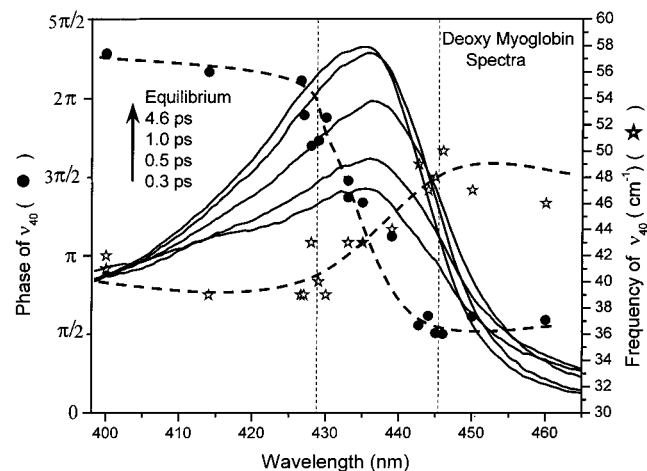
Figure 4. Phase (filled circles) and frequency (stars) profiles for ν_{40} in deoxy Mb are plotted as function of the pump/probe carrier wavelength. The vertical dashed lines delineate the region of phase and frequency drift. The pump-induced transient absorption line shape of deoxy Mb is also depicted for four time delays (0.3, 0.5, 1, and 4.6 ps), along with the equilibrium absorption line shape.

for a homogeneous model. It is clear that the theoretical prediction using the inhomogeneous line shape is in good agreement with the experimental data. Note that the phase approaches the off-resonant limit of $\pi/2$ much more rapidly on the red side than on the blue side of the absorption maximum. This reflects the strong asymmetry in the absorption spectrum. The sharp phase jump at the absorption maximum (435 nm) between $-\pi/2$ to $+\pi/2$ predicted by the homogeneous model is not observed in the experimental data. Also, contrary to the prediction of the homogeneous model, the experiment does not show a clear dip the amplitude of the 220 cm^{-1} mode near the absorption maximum. These observations are consistent with the assignment of the 220 cm^{-1} mode to a ground state coherence and strongly support the presence of significant inhomogeneous broadening in the Soret band of deoxy Mb. If the 220 cm^{-1} coherence originated from the excited state rather than the ground state, an amplitude dip and phase flip should be observed but slightly red-shifted from the emission maximum.[49] In fact, such phase behavior has been reported[32] for the reaction driven 220 cm^{-1} coherence of MbNO (which is effectively an excited-state coherence).

We now turn to the behavior of ν_{40} in deoxy Mb. In contrast to the high-frequency oscillations at 220 cm^{-1}, the frequency of ν_{40} seems to vary over the range 40–48 cm^{-1} as the pump/probe carrier wavelength is tuned to the red of the Soret absorption band. This is depicted in Figure 4, where we plot the measured frequencies along with the open band phase profiles. In addition to the systematic frequency drift (star symbols), we see that the phase profile (solid dots) also exhibits a strikingly different behavior from the predictions of the linearly displaced harmonic model shown in Figure 3. Rather than remaining a constant, the phase continually drifts over a range of about 2π in the 430–444 nm region.

B. Photochemically Active Samples. So far, we have been mainly concerned with nonreactive compounds, where the vibrational coherences are driven by the electric field interventions of the ultrafast pump laser pulse. Another important characteristic of time-resolved FCS is its ability to monitor chemical reactions and the subsequent evolution of the nonequilibrium product state. In this section, we present FCS experiments on a variety of photochemically active samples. The experimental data for some of these samples is plotted along

with the LPSVD fits and power spectra in Figures 5–7. The most distinguishing feature of the results in Figures 5–7, compared to the nonreactive samples, is the presence of a second mode at ~80 cm^{-1} (and sometimes higher harmonics at ~120 cm^{-1} and ~160 cm^{-1}), in addition to the low-frequency mode near 40 cm^{-1}. The mode near 80 cm^{-1} is significantly enhanced relative to ν_{40} when detuned detection conditions are employed,[32,42,49] and as a result, ν_{80} was emphasized in earlier studies[6] conducted under such conditions.

The frequencies of ν_{40} and ν_{80} for various photoreactive heme samples are presented in Table 1. Both ν_{40} and ν_{80} show slight sample dependent variations in frequency, but the higher frequency mode remains approximately twice the frequency of the low-frequency mode. The frequency pairs observed are 41–81 cm^{-1} in MbNO, 46–91 cm^{-1} in HbNO, 44–89 cm^{-1} in ferrous cytochrome *c*, 43–87 cm^{-1} in NO-bound H93G Mb, and 44–91 cm^{-1} in CO-bound FePPIX. The fact that the higher frequency oscillations near 80 cm^{-1} are approximately twice the frequency of the oscillations near 40 cm^{-1} is suggestive of a harmonic sequence. In the case of MbNO, it appears that even higher harmonics are present at 122 and 165 cm^{-1} (see top panel of Figure 7 and previous reports).[12,32]

Furthermore, the low-frequency oscillations seen in the MbNO sample near 40 cm^{-1} exhibit a continuous drift from 40 to 46 cm^{-1}, as the laser carrier wavelength is tuned toward the red (450–470 nm) of the product state (deoxy Mb) Soret absorption band. This frequency drift is shown in the upper panel of Figure 6 and follows the same general pattern observed for the field driven coherence in deoxy Mb (Figure 4). Note that, as for different heme samples, the frequency of the oscillations near 80 cm^{-1} remains approximately twice the frequency of the 40 cm^{-1} mode. These observations strongly suggest that ν_{80} forms part of a harmonic progression with ν_{40} as the fundamental frequency.

Another example of photochemical activity is ferrous cytochrome *c*, which was recently shown[54] to undergo a rapid ligand (methionine) photodissociation reaction followed by ~6 ps geminate rebinding. The oscillatory part of the FCS signal of ferrous cytochrome *c* is presented at four different carrier wavelengths in the first four panels of Figure 5, along with the corresponding LPSVD power spectra. The main features observed in the signal are a damped ~44 cm^{-1} oscillation (ν_{40}) and a ~89 cm^{-1} oscillation (ν_{80}) of smaller amplitude. Both of these modes exhibit a π phase flip and a dip in amplitude around 423 nm, which is close to the product state transient absorption maximum near 425 nm (known from white light continuum experiments).[54] The amplitude of ν_{80} seems to decrease faster than ν_{40} as the laser pulse carrier wavelength approaches 423 nm. The data generated at 423 nm are not shown because of the lack of an oscillatory signal. The ~44 and ~89 cm^{-1} oscillations used in the LPSVD fit to the data are depicted as solid and dashed lines, respectively (shifted from the data for clarity). The two vertical lines going through all panels are helpful in comparing the relative phases of the oscillatory components. An important observation is the coincidence of the ~89 cm^{-1} oscillation maxima or minima with the maxima and minima of the ~44 cm^{-1} oscillation and the fixed relative phase at all carrier wavelengths.

Turning back to MbNO, we present in Figure 6 the phase profiles of ν_{40} and ν_{80}, as the laser carrier frequency is varied across the Soret absorption region from 400 to 480 nm. The phase behavior of the two modes is very similar and their relative phase tracks together across the studied spectral region. The amplitude of ν_{80} is very small in the 420–435 nm region,
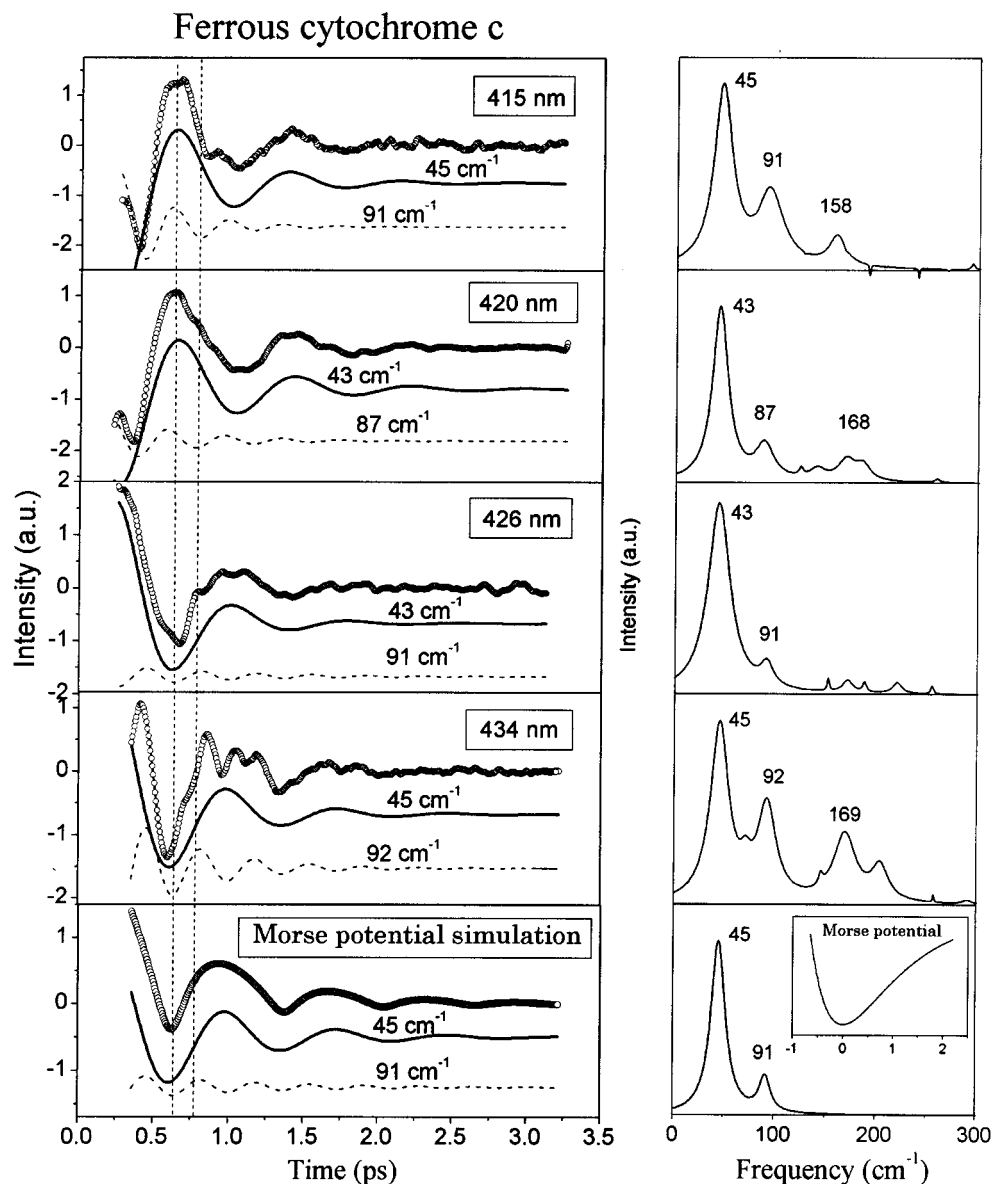
Figure 5. Sequence of experiments using the open band detection scheme on ferrous cytochrome *c* for four pump/probe carrier wavelengths. The left panels present the oscillatory part of the signal, and the right panels show the corresponding power spectra. The ∼44 cm^{-1} oscillation (solid line) and the ∼89 cm^{-1} oscillation (dashed line) used in the fit are shown displaced from the data. One can observe a π phase flip for both modes in the 420−426 nm spectral region. The left lower panel displays the simulated signal generated by the dynamics of a particle in a Morse potential $[U_g(q) = e^{-2q} - 2e^{-q}]$, along with the 45 and 91 cm^{-1} oscillations used for its fit. The lower right panel presents the associated power spectrum and a plot of the Morse potential (in the inset).

such that the corresponding phases are difficult to extract and hence not plotted for this wavelength region. We also plot the ratio of the amplitudes of the two modes, I_{80}/I_{40}, in the lower panel of Figure 6. The dip of the amplitude ratio near 427 nm is evident.

The oscillatory parts of the open band FCS signals in three different photochemically active samples (MbNO, NO-bound H93G Mb, and CO-bound FePPIX + 2MeIm) are displayed in Figure 7, along with the corresponding power spectra. The CO-bound FePPIX model complex was studied using a lower repetition rate amplified laser system[33] so that sample reset would be assured between the arrival of the pump/probe pulse pairs. The ν_{40} and ν_{80} oscillations used in fitting the data are depicted as solid and dashed lines (shifted for clarity). The Fe−His mode is found near 220 cm^{-1} in the power spectrum when the protein material is present and is downshifted to 211 cm^{-1} for the FePPIX model complex.[55] The low-frequency modes present in the power spectra of MbNO (upper right panel in

Figure 7) seem to form a four-term harmonic sequence (41, 82, 123, 164 cm^{-1}). This harmonic sequence is present in numerous data sets generated using MbNO.[12,32]

IV. Discussion

The technique of FCS is very useful for monitoring the nuclear motions associated with biomolecular reaction dynamics, especially in the low-frequency region of the vibrational spectrum. We have documented the presence of a mode near 40 cm^{-1} (ν_{40}) in all of the photostable heme proteins studied except cobalt-substituted Mb. In addition, we have found that the photochemically active heme samples display a harmonic progression involving this mode. The frequency, phase, and amplitude dependence of ν_{40} and ν_{80} were studied for deoxy Mb, MbNO, and ferrous cytochrome *c* as a function of the pump/probe carrier wavelength.

A. Phase and Frequency of ν_{40}. For deoxy Mb, we observe a discrepancy between the phase behavior of ν_{40} and the
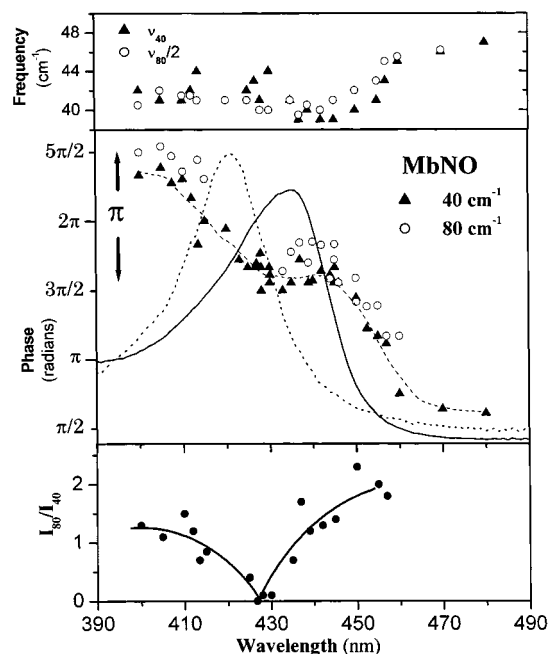
Figure 6. Upper panel displays the frequency of ν_{40} and ν_{80} in MbNO, as the pump/probe carrier wavelength is scaned over the 400–480 nm spectral region. Half the frequency of ν_{80} is plotted to facilitate its comparison with the frequency behavior of ν_{40}. The middle panel displays the phase behavior of ν_{40} (triangles) and ν_{80} (circles) modes in MbNO, along with the equilibrium absorption line shapes of MbNO (dashed line) and deoxy Mb (solid line). In the lower panel, the intensity ratio of ν_{80} and ν_{40} is displayed, showing a dip in the amplitude of ν_{80} near 427 nm.
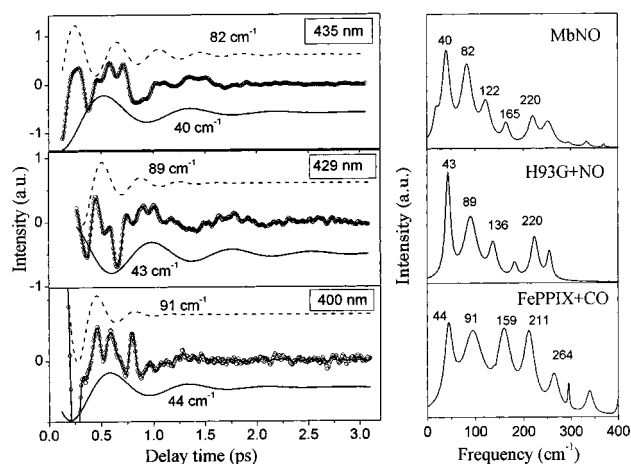

Figure 7. Sequence of experiments using the open band detection scheme on three photochemically active samples (MbNO, NO-bound H93G Mb, and CO bound FePPIX + 2MeIm). The left panels display the oscillatory part of the generated signal, and the right panels show the corresponding power spectra. The $\sim$40 cm^{-1} oscillation (solid line) and the $\sim$80 cm^{-1} oscillation (dashed line) used in the fit are shown displaced from the data. The relative damping of ν_{40} and ν_{80} can be compared by using the line widths of the power spectrum.

theoretical prediction[49] based on a simple linear harmonic model (cf. Figure 3b). In contrast to ν_{40}, the simple linear harmonic model (with inhomogeneous broadening) provides an excellent description of the phase behavior of the Fe–His mode at 220 cm^{-1}. One possible source for this discrepancy might have to do with the dynamic nature of the transient absorption line shape of photoexcited deoxy Mb. In Figure 4, we include the transient spectra measured using a white light continuum probe[48] at four different time delays (0.3, 0.5, 1.0, and 4.6 ps), along with the equilibrium absorption spectrum of Mb. The transient deoxy

Mb absorption band is broadened and initially located near 439 nm, which is toward the red side of the equilibrium absorption spectrum. The dynamics of the transient line shape consists of two major components, namely the narrowing of the spectrum and a shift to the blue as the system relaxes to equilibrium. The time scales for the transient line-shape dynamics (narrowing and blue shifting) are 0.4–4 ps and are attributed to the cooling and relaxation[48] of the hot deoxy Mb state created by the pump pulse. Since the picosecond line-shape dynamics take place on the same time scale as the low-frequency oscillations near 40 cm^{-1} (T_{40} = 0.8 ps), the shifting absorption maximum (439 → 435 nm) could conceivably affect the phase behavior of the detected oscillatory signals. Such anomalies might extend over a relatively broad range of carrier wavelengths, from $\sim$430 to $\sim$445 nm, due to the bandwidth ($\sim$5 nm) of the optical pulses and the inhomogeneity associated with deoxy Mb line shape. As seen in Figure 4, most of the anomalous phase drift for ν_{40} is localized within this spectral region, delineated by vertical dashed lines.

The drift of the frequency of ν_{40} as the carrier wavelength is tuned across the Soret absorption band (Figure 4) is probably linked to the inhomogeneities and protein-induced structural disorder of the heme system in deoxy Mb. As discussed earlier, the deoxy Mb absorption spectrum shows strong evidence of inhomogeneous broadening[26,27,51] and the highly asymmetric inhomogeneous line shape of Mb has been ascribed to disorder in the equilibrium position of the central iron atom.[26,27,51] This is of relevance to the low-frequency oscillations localized at the heme, which may involve the doming motion of the iron atom. Apart from a simple distribution in the equilibrium position of the heme iron,[27] the experimental data presented in Figure 4 suggest that the vibrational frequency of ν_{40} is also distributed. Thus, while the effect of inhomogeneities on the amplitude and phase excitation profiles of the 220 cm^{-1} mode appears only indirectly through the distribution in the electronic origins (Figure 3b), the ν_{40} frequency is evidently directly correlated with the electronic transition energy (i.e., with the disorder in the iron equilibrium position). This situation arises quite naturally if the protein conformation modulates *both* the equilibrium position and the curvature of the potential energy surface that governs the heme doming motion. When the carrier wavelength of the pump/probe pulse is tuned across the absorption spectrum, different conformational species are optically selected that have Soret band optical transitions (associated with the iron displacement)[27] that are correlated with different doming frequencies (ν_{40}).

Another major topic addressed in this paper concerns the assignment of ν_{40} and ν_{80} and the question of whether these modes are part of a harmonic progression or are independent fundamentals. In early work,[6] which utilized detuned detection, we assigned ν_{80} as the doming mode. This assignment was based upon the fact that although ν_{40} appeared in the power spectrum,[6] it was essentially undetectable in the raw data. However, recent advances in detection technique[32,56] have made the existence of ν_{40} unequivocal and have revealed modes at even lower frequencies.[57] An important observation, which strongly indicates that ν_{80} is a harmonic of ν_{40}, is the fact that $\nu_{80} \approx 2\nu_{40}$ under a variety of conditions (e.g., as carrier wavelength is varied, or as the sample is changed). These results suggest that these two modes are not independent vibrational fundamentals and force us to look for theoretical models that are consistent with those observations.

B. Harmonic Model. In considering the possibility that the low-frequency progressions in Figures 5–7 constitute an over-

Low-Frequency Oscillations in Heme Proteins

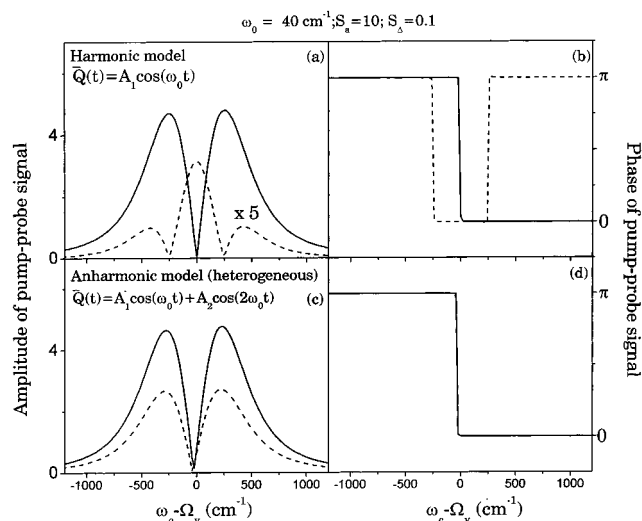*J. Phys. Chem. A, Vol. 106, No. 14, 2002* **3547**

Figure 8. Comparison of the open band amplitude and phase profiles for a harmonic and anharmonic oscillator model. Panels a and b show the open band amplitude and phase profiles for the fundamental (solid) and overtone (dashed) signals for a 40 cm^{-1} mode coupled to a two electronic level system. Panels c and d show the corresponding profiles for an anharmonic model that approximates the mean position of the oscillator $Q(t)$ to be adequately described by the first two harmonics of the Fourier series, with amplitudes A_1 (solid) and A_2 (dashed). For both the simulations, the nonstationary state was assumed to be a thermal state displaced from equilibrium.

tone or harmonic sequence, one can eliminate a simple linearly displaced harmonic oscillator model. Calculations[49] based on the linearly displaced harmonic model, where the main source of overtone intensity comes from the "double pass" of the wave packet across the probe detection region, predict that the intensities of the overtones are generally much smaller than the fundamental signals, as seen in the upper left panel of Figure 8. The double pass contribution can be understood through the time-dependent first moment of the vibrational coordinate that modulates the centroid of the equilibrium absorption spectrum. For example, consider a single mode coupled to a two electronic level system, with frequency ω_0 and electron−nuclear coupling force f. The pump interaction drives the nuclei out of equilibrium. If we let the time-dependent mean nuclear position after the pump interaction be $\langle Q(t) \rangle$, the correlation function that describes the response of the pump-induced nonstationary system can be shown to be of the form[49]

$$C_{\text{neq}}(t,t') = K(t-t') \exp\left[\left(\frac{if}{\hbar}\right)\int_{t'}^{t} ds \langle Q(s) \rangle \right] \quad (1)$$

where $K(t-t')$ is a correlation function (also called the optical absorption correlator) that describes the equilibrium line shape of the system. For a harmonic potential, the mean position $\langle Q(t) \rangle$ oscillates only at the fundamental frequency. In this case, the centroid of the nonequilibrium line shape induced by the pump pulse oscillates about the equilibrium absorption maximum at the fundamental oscillator frequency. It is then clear that the amplitude of the fundamental signal is proportional to the derivative of the absorption line shape, so that the oscillatory amplitude is largest near the shoulders of the absorption spectrum but vanishes at band center. On the other hand, the overtone amplitude profile is related to the second derivative of the absorption spectrum and naturally exhibits a contrasting behavior from the fundamental. [Here we ignore the very small contributions from the higher moment, i.e., $\langle Q^2(t) \rangle$ "squeezed" modulations, of the pump-induced vibrational wave packet.[58]]

As seen in the upper left panel of Figure 8, the overtones are peaked at the resonant absorption maximum, where the wave packet passes twice per period of oscillation, and exhibit an amplitude dip at two points near the shoulders of the absorption spectrum. Within this simple homogeneous harmonic model,[49] the fundamental and overtone phase profiles exhibit a π phase change associated with every dip in amplitude, generating the different phase behavior displayed in the upper right panel of Figure 8. This behavior is clearly not observed for ν_{40} and ν_{80} in the experimental results reported here (see Figures 5 and 6), where the two modes have nearly equivalent intensities and display similar phase and amplitude profiles.

C. Anharmonic Models. On the other hand, if we consider an asymmetric anharmonic potential for the low-frequency mode, we can explain many of the features observed in the experimental data. The assumption that the motion associated with ν_{40} takes place in an asymmetric anharmonic potential is quite reasonable, considering that the iron atom is coordinated only to the histidine on the proximal side, following the pump-induced ligand photodissociation reaction. As an example, we take the rescaled Morse potential plotted in the inset in the lower right panel of Figure 5. The potential is given by

$$U_{\text{g}}(q) = D_{\text{e}}[1 - e^{-aq}]^2 \quad (2a)$$

$$U_{\text{g}}(q) = (e^{-2q} - 2e^{-q} + 1) \quad (2b)$$

with a restoring force:

$$F(q) = -\frac{\partial U_{\text{g}}}{\partial q} = 2(e^{-2q} - e^{-q}) \quad (3)$$

where $q = Q - Q_0$ is the displacement from equilibrium and D_{e} and a, which scale U_{g} and q, are taken to be unity. The classical equation of motion for q is given by

$$m\ddot{q} = F(q) - \gamma_{\text{int}}\dot{q} \quad (4)$$

where $\dot{q}$ is the velocity and $-\gamma_{\text{int}}\dot{q}$ is the velocity dependent damping term. In Figure 9, we give a working example of the anharmonic potential. The factor $-\gamma_{\text{int}}\dot{q}$ in the expression for coordinate motion can be taken to represent the intrinsic homogeneous damping (due to population decay).

To simulate the first moment dynamics of the position coordinate associated with vibrational oscillations in an anharmonic potential, we place a particle in the Morse potential with a large initial displacement (which justifies the classical description). We then follow the dynamics induced by the restoring force $F(q)$ and the intrinsic damping. The simulated oscillatory signal for the homogeneous anharmonic model and the corresponding LPSVD power spectrum are presented in the upper panel of Figure 9. In this case, the only source of signal decay is the inherent damping present in the expression for coordinate motion ($-\gamma_{\text{int}}\dot{q}$).

For small initial displacements, the Morse potential can be well approximated as a harmonic potential and the dynamics resembles a simple damped harmonic oscillator. However, higher harmonics are needed to fit the simulated dynamics for large displacements. The relative amplitude of these higher harmonics (compared to the fundamental) increases as the initial displacement gets larger and the particle samples more anharmonic regions of the Morse potential. The intrinsic damping tends to decrease the amplitude of the oscillations so that the particle returns to regions of the potential closer to the equilibrium position, associated with higher frequencies. As a
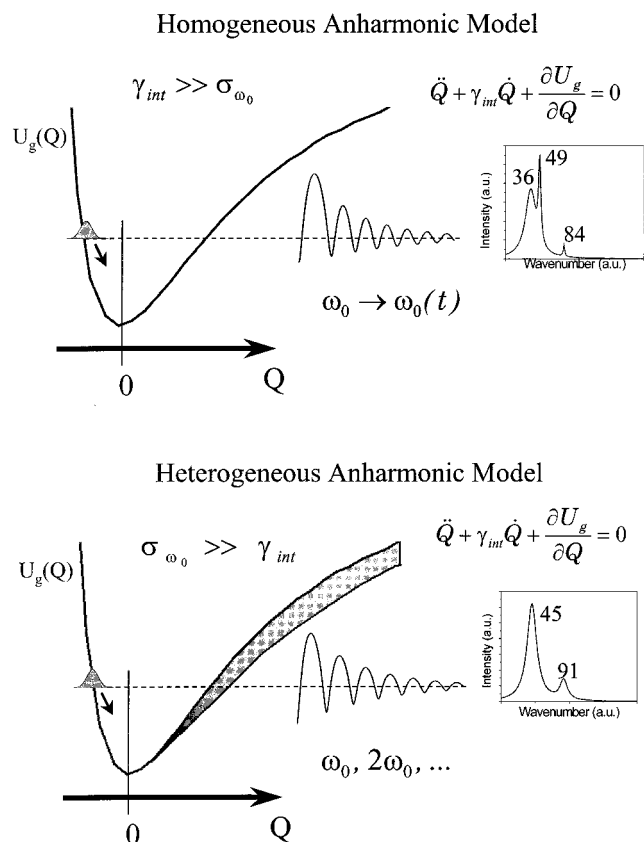
Homogeneous Anharmonic Model

$$\gamma_{int} \gg \sigma_{\omega_0}$$

$$\ddot{Q} + \gamma_{int}\dot{Q} + \frac{\partial U_g}{\partial Q} = 0$$

$U_g(Q)$

$$\omega_0 \rightarrow \omega_0(t)$$

Heterogeneous Anharmonic Model

$$\sigma_{\omega_0} \gg \gamma_{int}$$

$$\ddot{Q} + \gamma_{int}\dot{Q} + \frac{\partial U_g}{\partial Q} = 0$$

$U_g(Q)$

$$\omega_0, 2\omega_0, \ldots$$

Figure 9. Signals simulated using the dynamics of a particle initially displaced on a Morse potential [$U_g(q) = e^{-2q} - 2e^{-q}$], as well as the corresponding power spectra, are presented considering two sources of damping. In the upper panel we consider the inherent homogeneous population damping ($\gamma_{int} \gg \sigma_{\omega_0}$) which is analogous to "friction" on the potential surface. Due to the decreasing oscillatory amplitude in the anharmonic potential, the simulated signal contains time dependent frequencies, which are fit with LPSVD using two damped cosine functions with different lifetimes. In the lower panel, the damping factor is introduced as an inhomogeneous frequency distribution ($\sigma_{\omega_0} \gg \gamma_{int}$), which is associated with pure dephasing and/or different potential curvatures. The signal simulated using the heterogeneous anharmonic model is fit by LPSVD with a damped fundamental oscillation and its higher harmonics.

result, for large initial displacements, the oscillatory frequency effectively becomes time dependent [$\omega_0 \rightarrow \omega_0(t)$], starting at lower frequencies and evolving toward higher frequencies as the system damps (see simulated signal in the upper panel of Figure 9). The LPSVD algorithm fits such a signal with a low frequency and short lifetime component (e.g., 36 cm^{-1}) for the early time signal and with a longer-lived higher frequency component (e.g., 49 cm^{-1}) for the signal at later times. This generates the power spectrum presented in the inset of the upper panel of Figure 9. Since the experimental signals do not display a time-dependent oscillatory frequency (i.e., a single peak in the power spectrum is sufficient to fit the fundamental oscillation), we are led to an anharmonic model where damping due to the inhomogeneous nature of the system is explicitly considered.

The experimentally observed oscillatory signals can be damped by sources other than population decay. For example, the protein conformational substates discussed earlier lead to correlated distributions of heme out-of-plane geometry and doming frequency. The distribution of vibrational frequencies will broaden the spectral line as well as damp the oscillatory signals. We also note that, since the oscillatory frequency in an anharmonic potential depends on the initial displacement,

conformational inhomogeneities can induce a distribution of frequencies through either a distribution of initial displacements or through a distribution in the shape (curvature) of the potential (or both). Finally, if the protein and/or solvent undergo structural fluctuations on faster time scales, pure dephasing[59] (bath induced energy level fluctuations) will result, which is another form of line broadening without population decay.

As an example, a distribution in the curvature of the potential is presented in the lower panel of Figure 9. In this heterogeneous anharmonic model, the inhomogeneous broadening (or pure dephasing) is considered to be larger than the intrinsic damping due to population decay ($\sigma_{\omega_0} \gg \gamma_{int}$). To generate the simulated signal within this model, we allow the system to evolve on the anaharmonic potential with small inherent damping ($-\gamma_{int}\dot{q}$). For the dynamics generated under these conditions, the amplitude of oscillations and, hence, the fundamental oscillatory frequency remain almost constant in time. This means that the coordinate $Q(t)$ can be well described using a Fourier series involving only the fundamental frequency and its higher harmonics ($\omega_0, 2\omega_0, \ldots$). The final simulated signal is generated by convolving the dynamics of a single protein molecule over a frequency distribution that is commensurate with the experimentally observed peak width in the power spectrum ($\sim$12 cm^{-1}).

Within this model, we write the signal for a single undamped anharmonic oscillator as a Fourier series:

$$S_h(\omega_0, \omega_c, \tau) = \sum_{n=1}^{\infty} A_n \cos(n\omega_0\tau + \phi_n) \tag{5}$$

Here, the summation is over all the harmonics of the fundamental mode frequency ω_0, and the optical carrier frequency dependence of the final signal is denoted by ω_c. For simplicity, we assume that, for a narrow frequency distribution, the amplitudes A_n of the various overtones do not depend on the mode frequency. If the inhomogeneous vibrational distribution is specified by a mean vibration frequency $\bar{\omega}_0$ and a function $f(\bar{\omega}_0 - \omega_0)$, the final signal is obtained from a simple convolution of the above expression with the inhomogeneous distribution:

$$S_I(\bar{\omega}_0, \omega_c, \tau) = \int d\omega_0 f(\bar{\omega}_0 - \omega_0) S_h(\omega_0, \omega_c, \tau) \tag{6}$$

The observed signal is well described by this model, using a fundamental oscillation and its higher harmonic, as seen in the associated LPSVD power spectrum in the lower panels of Figures 5 and 9. However, the damping associated with inhomogeneous broadening can have somewhat stronger effects on the decay times of the higher harmonics. In contrast, pure dephasing affects the damping of the fundamental and its harmonics in a similar fashion. Since the lifetime observed for ν_{80} in ferrous cytochrome c, MbNO, and HbNO is comparable to the lifetime of ν_{40}, we infer that the damping of the low-frequency signals probably involves some degree of pure dephasing, along with enough inhomogeneous broadening to account for the frequency drift of ν_{40} shown in Figure 4.

If we consider an anharmonic potential for the vibrational coordinate, the first moment modulation $\langle Q(t) \rangle$ in eq 1 directly contains the higher harmonics of the fundamental frequency. Consequently, the centroid of the line shape is modulated at the higher harmonics, as well as at the fundamental frequency. The amplitude and phase profiles of such harmonics, when detected in a pump/probe experiment, are expected to track the amplitude and phase profile of the fundamental, i.e., the

amplitudes dip and their phase flips by π at the absorption maximum. This is illustrated in the lower panels of Figure 8.

The presence of a π phase flip and amplitude dip in ferrous cytochrome *c* around 423 nm for both ν_{40} and ν_{80} (see Figure 5) agrees well with the predictions made using the above model. We have used a Gaussian frequency distribution equivalent to a $\sim$12 cm^{-1} inhomogeneous broadening of the 45 cm^{-1} mode to generate the simulated signal presented in the lower panel of Figure 5. The simulations look very similar to the oscillatory signal measured in ferrous cytochrome *c* at 426 and 434 nm presented in the third and fourth panels (and to the signal measured at 415 and 420 nm when the π phase shift is added). The similarity is connected to the fixed relative phase relation between ν_{40} and ν_{80} in the experimental and simulated data as seen in Figure 5. The alignment of the maxima and minima of these oscillatory components is the key condition needed to generate the pattern observed in the experimental data. The good agreement, observed between the experimental data for ferrous cytochrome *c* and the simulations, makes a strong case for a description of the nuclear coordinate motion using an anharmonic potential surface.

Similar behavior is observed for ν_{40} and ν_{80} in MbNO, as displayed in Figure 6. The 80 cm^{-1} mode displays a phase flip and a dip in amplitude near 427 nm. The phase of the 40 cm^{-1} mode presents a slower π phase shift in the 427 nm region, which is not associated with a clear dip in amplitude. This observation is anomalous and may signal the presence of more complex electron−nuclear coupling (e.g., quadratic coupling), which can shift the phase and amplitude transition points away from the absorption maximum.[49] The phase drift observed in the 445−480 nm region for both the ν_{40} and the ν_{80} modes in MbNO (Figure 6) is probably correlated to the frequency drift displayed in the same spectral region. The carrier wavelength dependence of both the frequency and phase may be related to the underlying inhomogeneity associated with the deoxy Mb Soret band. Thus, the carrier wavelength may resonantly select a subpopulation of conformational states that have different values of ν_{40}. Such a scenario is consistent with the concept of a distribution of anharmonic potential surfaces that is correlated with the distribution of electronic transition energies.

D. Alternative Models. An alternative possibility is a model recently proposed[60] to account for the anomalous phase and amplitude behavior of the 47 cm^{-1} mode, observed in studies of the ultrafast photodissociation of CO from cytochrome oxidase. This proposal suggests that sequential population transfer from the CO bound to the CO unbound state takes place as the heme oscillates (domes) with a period of 700 fs. The unusual phase and amplitude excitation profiles observed for the 47 cm^{-1} mode of cytochrome oxidase resemble the observations presented here for ν_{40} in Mb and are used by Liebl et al.[60] to rationalize the coherent population transfer model. However, we also see clear evidence for ν_{40} in deoxy Mb, where no reaction or population transfer event is taking place (see Figure 2). Thus, it appears that ν_{40} represents a genuine vibrational coherence, and the coherent population transfer model[60] can be eliminated from consideration (at least for Mb). The observation of ν_{40} in more sophisticated wavelength-selective modulation experiments[57] on MbNO, which experimentally discriminate against population transfer signals, is also inconsistent with a coherent population transfer model for NO photodissociation.

The basic assignment (see below) of ν_{40} and ν_{80} to heme doming[6,12,32] is in accord with the conclusions of Liebl et al.[60] However, we differ on the physical mechanism that generates the oscillatory signal. We suggest that the signal is a genuine vibrational coherence, triggered by the electron rearrangements associated with ligand photodissociation, and that a heterogeneous, anharmonic model, analogous to the one presented in the lower portion of Figure 9, is the key to a quantitative understanding of the observations.

E. Anharmonic Mode Assignments. Through the study of a wide variety of heme proteins and model compounds, we have shown that ν_{40} involves the core of the porphyrin macrocycle and is affected by the replacement of the heme iron atom with cobalt. This strongly suggests that ν_{40} is connected to the heme doming motion. The possibility of a purely electronic coherence, associated with the low-lying spin states of the ferrous heme iron atom cannot be completely excluded at this time. However, such an assignment is difficult to reconcile with the presence of ν_{40} in both the ferric and ferrous species and with the appearance of the ν_{80} harmonic only in the photolytically excited samples. These observations, along with recent normal mode calculations,[29−31] which predict the doming frequency near 50 cm^{-1}, strongly support a doming assignment for ν_{40} and ν_{80}. Moreover, the force constant previously estimated[25−27] from ligand rebinding kinetics ($K \approx 15$ N/m) also predicts a doming frequency on the order of 50 cm^{-1}. The large initial displacements needed within an anharmonic potential model to generate the observed higher harmonics, along with the presence of harmonics such as ν_{80} in the photochemically active samples, suggest that ν_{40} is a key fundamental oscillation that is directly coupled to the reaction coordinate. The iron motion associated with heme doming, from the in-plane position in the ligand bound state of Mb to the out-of-plane displaced position ($\sim$0.4 Å) for the unligated state,[25−30] provides the large initial displacements needed for the appearance of the higher harmonics in a Fourier series description of the anharmonic coordinate motion. As a result of the above considerations, we propose that ν_{40} and ν_{80} are a direct reflection of the anharmonic potential that describes the heme doming motion and that the damping of the oscillatory signals arises from inhomogeneity and/or pure dephasing effects.

The nearly equal spacing of the harmonic progression ($\nu_{80} \approx 2\nu_{40}$) may appear surprising for an anharmonic potential surface. However, for large displacements from equilibrium, the energy level spacing in an anharmonic Morse potential becomes nearly linear in quantum number for the lower harmonics. This is consistent with the classical wave packet description of the anharmonic motion [i.e., the Fourier series describing $\langle Q(t) \rangle$ will always contain integer multiples of the fundamental frequency]. For the Morse oscillator, the expressions are analytic, since the energy eigenvalues are given by

$$E_n = \left(n + \left(\frac{1}{2}\right)\right)\hbar\omega - \left(n + \left(\frac{1}{2}\right)\right)^2 \hbar\omega x_e \qquad (7a)$$

with

$$x_e = \frac{a^2\hbar}{2m\omega} \qquad a = \sqrt{\frac{m}{2D_e}}\omega \qquad (7b)$$

so that

$$E_{n+s} - E_n = s\hbar\omega[1 - (2n+1)x_e - sx_e] \approx s\hbar\omega[1 - 2nx_e] \quad (8)$$

which is linear in s for $n \gg s$. The linear relation implies that the lower harmonics (small *s*) at large displacement (large *n*) will be integral multiples of the "fundamental" frequency $\omega[1 - 2nx_e]$.
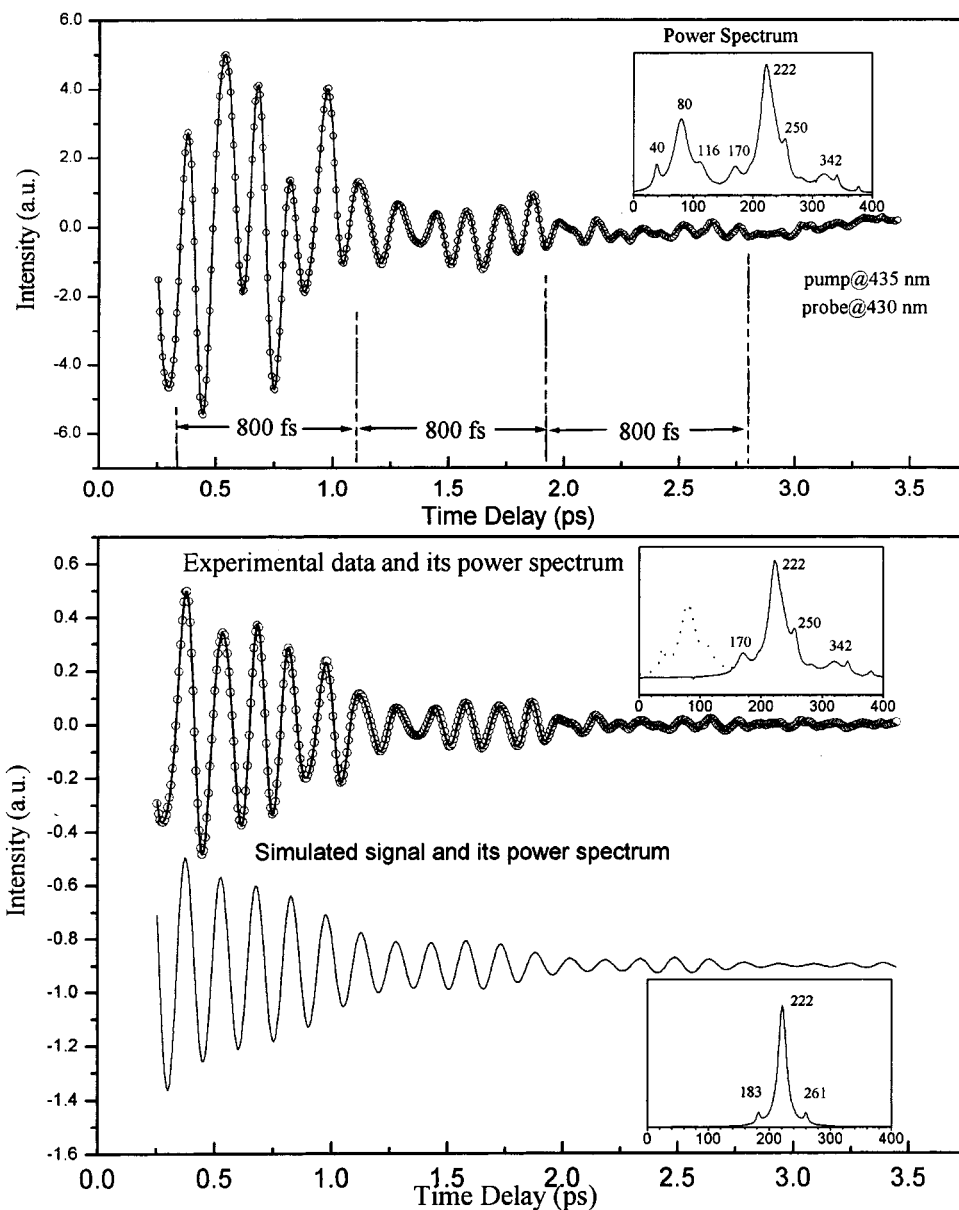
Figure 10. Upper panel displays the oscillatory signal from MbNO-generated using the detuned detection scheme (pump/probe carrier wavelength at 435 nm, detection at 430 nm, for ~60 fs pulses). The vertical dashed lines, defining 800 fs intervals, help one follow the sequential damping of the 220 cm^{-1} mode. The inset shows the corresponding power spectrum. The lower panel displays the same experimental data as the upper panel, after the lower frequency modes (shown by the dashed line in the associated power spectrum) have been subtracted. A simulated signal in which the damping of a 220 cm^{-1} oscillatory signal is modulated by a 40 cm^{-1} oscillation is also shown. The expression used for the simulation is $S_{SIM} = \cos(\omega_{220}t) \cdot \exp(-\gamma t) \cdot \exp(-\Delta\gamma t(1 - \cos(\omega_{40}t)))$ where $\gamma = (775 \text{ fs})^{-1}$ and $\Delta\gamma = (5.2 \text{ ps})^{-1}$. The last inset shows the power spectrum associated with the simulated signal. The sequential damping of the 220 cm^{-1} oscillations adds two sidebands (at 183 and 261 cm^{-1}) to the power spectrum with an appropriate relative phase.

F. Mode Coupling and Damping Effects. The assignment of ν_{40} and ν_{80} to the heme doming motion is also in agreement with the data presented in Figure 10, which is suggestive of coupling between ν_{Fe-His}, at 220 cm^{-1}, and the ν_{40} mode. The upper panel of Figure 10 displays the oscillatory signal generated using detuned detection[32] to enhance the high-frequency portion of the reaction driven coherence in MbNO. The corresponding power spectrum is presented in the inset. The dominating feature in the data is the 220 cm^{-1} oscillation associated with the Fe−His mode. An interesting observation is the sequential damping of the 220 cm^{-1} oscillations. The oscillations have almost the same amplitude for the initial ~800 fs, after which the amplitude drops and remains almost constant for the next ~800 fs, and so on, until they damp out. Since the period of oscillation of the 40 cm^{-1} mode is 800 fs, we infer that the damping of the

220 cm^{-1} oscillations might be modulated by the motion associated with the 40 cm^{-1} mode. In the lower panel of Figure 10, we display the same experimental data as in the upper panel, after subtracting the modes below 150 cm^{-1} (plotted with dashed line in the second inset). Below, we display a simulated signal that resembles the experimental data, along with its LPSVD generated power spectrum. The expression used to generate the simulated signal contains a 220 cm^{-1} mode whose damping is modulated by the 40 cm^{-1} mode:

$$S_{SIM}(t) = e^{-t[\gamma_0 + \Delta\gamma(1 - \cos\omega_{40}t)]} \cos\omega_{220}t \qquad (9)$$

where ω_{220} and ω_{40} are the angular frequencies of the 220 and 40 cm^{-1} modes. The damping factor consists of the regular

Low-Frequency Oscillations in Heme Proteins

J. Phys. Chem. A, Vol. 106, No. 14, 2002 **3551**

exponential decay term, $e^{-\gamma_0 t}$, to which we add a term representing the effect of the 40 cm^{-1} mode on the overall damping:

$$\exp[-\Delta\gamma t(1 - \cos \omega_{40} t)] \qquad (10)$$

such that the time-dependent damping factor becomes

$$\gamma(t) = \gamma_0 + \Delta\gamma(1 - \cos \omega_{40} t) \qquad (11)$$

The good agreement between the experimental data and the simulations generated by such a simple theoretical expression suggests that there is coupling between the Fe−His and the ν_{40} doming modes. The presence of such coupling is reasonable since both modes involve the iron motion. For example, when the iron atom displacement passes through the maximum out-of-plane position, the Fe−His mode might couple more efficiently with in-plane heme modes (leading to stronger damping of $\nu_{\text{Fe}-\text{His}}$). When the iron atom is undisplaced and the Fe−His mode involves motion that is strictly orthogonal to the heme plane there would be less coupling to in-plane modes and subsequently less damping.

An alternative explanation of the pattern observed in Figure 10 could involve the beating between the Fe−His mode (relative amplitude given by A) and two sideband modes (located at $\sim\pm40$ cm^{-1}). However, the phases of all three modes would have to be (coincidently) locked into a specifically required relationship in order to generate the observed oscillatory pattern. Using the expression

$$\cos(\omega_{260}t + \varphi_{220} + \varphi_{40}) + \cos(\omega_{180}t + \varphi_{220} - \varphi_{40}) +$$
$$2A \cos(\omega_{220}t + \varphi_{220}) =$$
$$2 \cos(\omega_{220}t + \varphi_{220})[A + \cos(\omega_{40}t + \varphi_{40})] \quad (12)$$

we derive the relationship between the phases ($\varphi_{260} = \varphi_{220} + \varphi_{40}$ and $\varphi_{180} = \varphi_{220} - \varphi_{40}$) of the two sidebands and the 220 cm^{-1} mode to be $\varphi_{260} + \varphi_{180} = 2\varphi_{220}$. Since we consider such a coincidence to be highly unlikely, the coupling between the doming and Fe−His modes remains as an intriguing source of vibrational damping in this system.

In contrast to the $\nu_{\text{Fe}-\text{His}}$ mode, which may damp by coupling to the in-plane heme vibrations, the damping of the 40 cm^{-1} doming motion is probably related to coupling between the heme and the protein. It has been well documented[19,21,23,28,48,61−67] that Mb undergoes structural rearrangements following the ligand photodissociation reaction. These rearrangements surely affect the characteristics of the heme active site, including the shape of the potential that governs the heme doming motion. One possibility is that, following the photolysis reaction, the iron atom initially feels a more anharmonic potential that evolves, due to the protein relaxation dynamics, toward a more harmonic potential, associated with the equilibrium structure of deoxy Mb. In Figure 11, we display two example potential surfaces for the iron doming motion. The first one arises immediately after the photolysis reaction (solid line) and, at 300 K, evolves on a picosecond (τ_R) time scale toward the more harmonic surface (dashed line) associated with the relaxed deoxy Mb state. For example, the steeper slope at small coordinate values in the early time potential surface could be due to steric hindrance between the proximal histidine and the porphyrin ring. The presence of ν_{80} in the reactive samples can be explained by the large initial displacements (and the anharmonic potential) associated with the dissociation reaction. The much smaller displacements and the more harmonic shape of the potential surface in the photostable samples explains the absence of ν_{80} and accounts for the similar value of ν_{40} in the photostable and
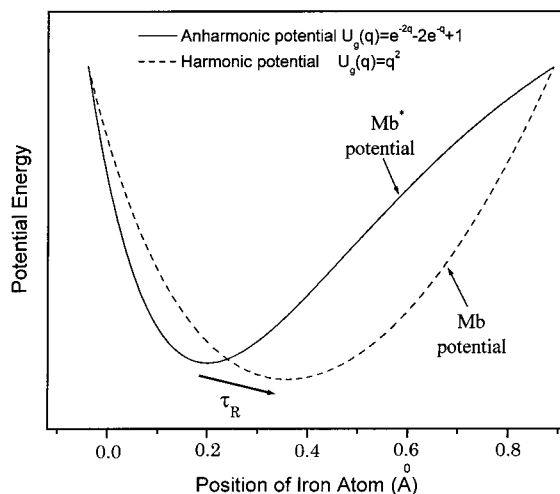

Figure 11. A time dependent potential surface can be associated with the forces acting on the iron atom following the ligand photodissociation. The surfaces for two pump/probe delay times, are displayed. The anharmonic potential (solid line) dictates the ν_{40} and ν_{80} dynamics immediately after the photodissociation reaction, before any protein structural rearrangements can take place. The more harmonic potential (dashed line) characterizes the ν_{40} dynamics for the relaxed structure of deoxy Mb. The evolution of the potential shape induced by the protein structural rearrangements is expected to take place on the picosecond time scale (τ_R).

photoactive samples. The early time potential can be associated with the state sometimes denoted as Mb*, which involves a deligated and partially relaxed heme surrounded by a protein that has not yet relaxed from the bound state configuration to its new set of equilibrium states. The relaxation of such states can, in principle, be observed using a combination of short time and low-temperature measurements, and we are currently exploring FCS studies in the low-temperature regime to probe the sensitivity of this technique to the protein/heme relaxation processes.

We note in closing that a mode analogous to ν_{40} has not yet been clearly observed[68] in recent high-resolution synchrotron based experiments on Mb, which are sensitive to the vibrational spectrum of the ^{57}Fe at the active site. A suppression of the intensity of this mode in the detected Fe density-of-states would be explained if the iron motion represents a relatively small fraction of the total kinetic energy involved in the ν_{40} motion. This would be the case if there were significant collective motions that involved the surrounding protein or solvent material when the heme domes.[68] A final possibility is that the motion associated with ν_{40} is more strongly damped below the glass transition, at the low temperatures used in the synchrotron experiments.

References and Notes

(1) Scherer, N. F.; Jonas, D. M.; Fleming, G. R. *J. Chem. Phys.* **1993**, *99*, 153−168.

(2) Pugliano, N.; Szarka, A. Z.; Hochstrasser, R. M. *J. Chem. Phys.* **1996**, *104*, 5062−5079.

(3) Chachisvilis, M.; Fidder, H.; Sundstrom, V. *Chem. Phys. Lett.* **1995**, *234*, 141−150.

(4) Polanyi, J. C.; Zewail, A. H. *Acc. Chem. Res.* **1995**, *28*, 119−132.

(5) Ziegler, L. D.; Fan, R.; Desrosiers, A. E.; Scherer, N. F. *J. Chem. Phys.* **1994**, *100*, 1823−1839.

(6) Zhu, L. Y.; Sage, J. T.; Champion, P. M. *Science* **1994**, *266*, 629−632.

(7) Vos, M. H.; Rappaport, F.; Lambry, J. C.; Breton, J.; Martin, J. L. *Nature* **1993**, *363*, 320−325.

(8) Ruhman, S.; Joly, A. G.; Nelson, K. A. *J. Chem. Phys.* **1987**, *86*, 6563−6565.

(9) Zewail, A. H. *Femtochemistry: Ultrafast Dynamics of the Chemical Bond*, World Scientific Publishing Co. Pte. Ltd.: Singapore, 1994.

(10) Wang, Q.; Schoenlein, R. W.; Peteanu, L. A.; Mathies, R. A.; Shank, C. V. *Science* **1994**, *266*, 422−424.

(11) Zhu, L. Y.; Wang, W.; Sage, J. T.; Champion, P. M. *J. Raman Spectrosc.* **1995**, *26*, 527−534.

(12) Champion, P. M.; Rosca, F.; Wang, W.; Kumar, A. T. N.; Christian, J.; Demidov, A. Laser Techniques for Condensed-Phase and Biological Systems. *Proc. SPIE* **1998**, *3273*, 80−89.

(13) Janes, S. M.; Dalickas, G. A.; Eaton, W. A.; Hochstrasser, R. M. *Biophys. J.* **1988**, *54*, 545−549.

(14) Ansari, A.; Jones, C. M.; Henry, E. R.; Hofrichter, J.; Eaton, W. A. *Biophys. J.* **1993**, *64*, 852−868.

(15) Jackson, T. A.; Lim, M.; Anfinrud, P. A. *Chem. Phys.* **1994**, *180*, 131−140.

(16) Kaminaka, S.; Ogura, T.; Kitagawa, T. *J. Am. Chem. Soc.* **1990**, *112*, 23−27.

(17) Lambright, D. G.; Balasubramanian, S.; Boxer, S. G. *Chem. Phys.* **1991**, *158*, 249−260.

(18) Nakabayashi, T.; Okamoto, H.; Tasumi, M. *J. Phys. Chem. A* **1997**, *101*, 3494−3500.

(19) Tian, W. D.; Sage, J. T.; Srajer, V.; Champion, P. M. *Phys. Rev. Lett.* **1992**, *68*, 408−411.

(20) Srajer, V.; Reinisch, L.; Champion, P. M. *Biochemistry* **1991**, *30*, 4886−4895.

(21) Sage, J. T.; Schomacker, K. T.; Champion, P. M. *J. Phys. Chem.* **1995**, *99*, 3394−3405.

(22) Walda, K. N.; Liu, X. Y.; Sharma, V. S.; Magde, D. *Biochemistry* **1994**, *33*, 2198−2209.

(23) Austin, R. H.; Beeson, K.; Eisenstein, L.; Frauenfelder, H.; Gunsalus, I. C. *Biochemistry* **1975**, *14*, 5355−5373.

(24) Carver, T. E.; Rohlfs, R. J.; Olson, J. S.; Gibson, Q. H.; Blackmore, R. S.; Springer, B. A.; Sligar, S. G. *J. Biol. Chem.* **1990**, *265*, 20007−20020.

(25) Srajer, V.; Reinisch, L.; Champion, P. M. *J. Am. Chem. Soc.* **1988**, *110*, 6656−6670.

(26) Srajer, V.; Champion, P. M. *Biochemistry* **1991**, *30*, 7390−7402.

(27) Champion, P. M. *J. Raman Spectrosc.* **1992**, *23*, 557−567.

(28) Perutz, M. F. *Proc. R. Soc. London B* **1980**, *208*, 135−162.

(29) Kozlowski, P. M.; Spiro, T. G.; Berces, A.; Zgierski, M. Z. *J. Phys. Chem. B* **1998**, *102*, 2603−2608.

(30) Spiro, T. G.; Kozlowski, P. M.; Zgierski, M. Z. *J. Raman Spectrosc.* **1998**, *29*, 869−879.

(31) Kozlowski, P. M.; Spiro, T. G.; Zgierski, M. Z. *J. Phys. Chem. B* **2000**, *104*, 10659−10666.

(32) Rosca, F.; Kumar, A. T. N.; Ye, X.; Sjodin, T.; Demidov, A. A.; Champion, P. M. *J. Phys. Chem. A* **2000**, *104*, 4280−4290.

(33) Wang, W.; Demidov, A. A.; Ye, X.; Christian, J. F.; Sjodin, T.; Champion, P. M. *J. Raman Spectrosc.* **2000**, *31*, 99−105.

(34) Gerber, N. C.; Sligar, S. G. *J. Biol. Chem.* **1994**, *269*, 4260−4266.

(35) Barrick, D.; Dahlquist, F. W. *Proteins: Struct., Funct., Genet.* **2000**, *39*, 278−290.

(36) Barrick, D. *Proteins: Struct., Funct., Genet.* **2000**, *39*, 291−308.

(37) Yonetani, T.; Yamamoto, H.; Woodrow, G. V. *J. Biol. Chem.* **1974**, *249*, 682−690.

(38) Neya, S.; Funasaki, N.; Sato, T.; Igarashi, N.; Tanaka, N. *J. Biol. Chem.* **1993**, *268*, 8935−8942.

(39) Mazumdar, S. *J. Chem. Soc., Dalton Trans.* **1991**, 2091.

(40) Wise, F.; Rosker, M.; Millhauser, G.; Tang, C. L. *J. Quantum Electron.* **1987**, *QE−23*, 1116.

(41) Kumar, A. T. N.; Zhu, L.; Christian, J. F.; Demidov, A. A.; Champion, P. M. *J. Phys. Chem. B* **2001**, *105*, 7847−7856.

(42) Constantine, S.; Zhou, Y.; Morais, J.; Ziegler, L. D. *J. Phys. Chem. A* **1997**, *101*, 5456−5462.

(43) Champion, P. M.; Lange, R. *J. Chem. Phys.* **1980**, *73*, 5947−5957.

(44) Adar, F.; Gouterman, M.; Aronowitz, S. *J. Phys. Chem.* **1976**, *80*, 2184−2191.

(45) Champion, P. M.; Perreault, G. J. *J. Chem. Phys.* **1981**, *75*, 490−491.

(46) Friedman, J. M.; Rousseau, D. L. *Chem. Phys. Lett.* **1978**, *55*, 488−492.

(47) Hochstrasser R. M. *Probes of Structure and Function of Macromolecules and Membranes*; Academic Press: New York, 1971; p 57.

(48) Demidov, A. A.; Ye, X.; Rosca, F.; Kumar, A. T. N.; Ionascu, D.; Wang, W.; Zhu, L.; Champion, P. M. Manuscript in preparation.

(49) Kumar, A. T. N.; Rosca, F.; Widom, A.; Champion, P. M. *J. Chem. Phys.* **2001**, *114*, 701−724.

(50) Kitagawa T. *Biological Applications of Raman Spectroscopy*; Wiley−Interscience Publication: New York, 1988; Chapter 3, pp 97−131.

(51) Srajer, V.; Schomacker, K. T.; Champion, P. M. *Phys. Rev. Lett.* **1986**, *57*, 1267−1270.

(52) Bangcharoenpaurpong, O.; Schomacker, K. T.; Champion, P. M. *J. Am. Chem. Soc.* **1984**, *106*, 5688−5698.

(53) Srajer, V. Ph.D. Thesis, Northeastern University, 1991.

(54) Wang, W.; Ye, X.; Demidov, A. A.; Rosca, F.; Sjodin, T.; Cao, W.; Sheeran, M.; Champion, P. M. *J. Phys. Chem. B* **2000**, *104*, 10789−10801.

(55) Desbois, A.; Momenteau, M.; Loock, B.; Lutz, M. *Spectroscopy Lett.* **1981**, *14*, 257−269.

(56) Rosca, F.; Ionascu, D.; Kumar, A. T. N.; Demidov, A. A.; Champion, P. M. *Chem. Phys. Lett.* **2001**, *337*, 107−116.

(57) Rosca, F.; Kumar, A. T. N.; Ionascu, D.; Sjodin, T.; Demidov, A. A.; Champion, P. M. *J. Chem. Phys.* **2001**, *114*, 10884−10898.

(58) Kumar, A. T. N.; Rosca, F.; Widom, A.; Champion, P. M. *J. Chem. Phys.* **2001**, *114*, 6795−6815.

(59) Tokmakoff, A.; Fayer, M. D. *Acc. Chem. Res.* **1995**, *28*, 437−445.

(60) Liebl, U.; Lipowski, G.; Negrerie, M.; Lambry, J. C.; Martin, J. L.; Vos, M. H. *Nature* **1999**, *401*, 181−184.

(61) Deak, J.; Chin, H. L.; Lewis, C. M.; Miller, R. J. D. *J. Phys. Chem. B* **1998**, *102*, 6621−6634.

(62) Friedman, J. M.; Scott, T. W.; Fisanick, G. J.; Simon, S. R.; Findsen, E. W.; Ondrias, M. R.; Macdonald, V. W. *Science* **1985**, *229*, 187−190.

(63) Petrich, J. W.; Martin, J. L.; Houde, D.; Poyart, C.; Orszag, A. *Biochemistry* **1987**, *26*, 7914−7923.

(64) Lingle, R.; Xu, X. B.; Zhu, H. P.; Yu, S. C.; Hopkins, J. B. *J. Phys. Chem.* **1991**, *95*, 9320−9331.

(65) Lim, M.; Jackson, T. A.; Anfinrud, P. A. *Proc. Natl. Acad. Sci. U.S.A.* **1993**, *90*, 8302.

(66) Causgrove, T. P.; Dyer, R. B. *Biochemistry* **1993**, *32*, 11985−11991.

(67) Ansari, A.; Jones, C. M.; Henry, E. R.; Hofrichter, J.; Eaton, W. A. *Science* **1992**, *256*, 1796−1798.

(68) Sage, J. T.; Durbin, S. M.; Sturhahn, W.; Wharton, D. C.; Champion, P. M.; Hession, P.; Sutter, J.; Alp, E. E. *Phys. Rev. Lett.* **2001**, *86*, 4966−4969.